# Supporting Information

## Assessing the drawbacks and benefits of ion migration in lead halide perovskites

Kostiantyn Sakhatskyi[1,2,#], Rohit Abraham John[1,2,#]*, Antonio Guerrero[3,#], Sergey Tsarev[1,2,#], Sebastian Sabisch[1], Tisita Das[4], Gebhard J. Matt[1,2], Sergii Yakunin[1,2], Ihor Cherniukh[1,2], Martin Kotyrba[1,2], Yuliia Berezovska[1,2], Maryna I. Bodnarchuk[1,2], Sudip Chakraborty[4], Juan Bisquert[3,5], Maksym V. Kovalenko[1,2]*

[1] Laboratory of Inorganic Chemistry, Department of Chemistry and Applied Biosciences, ETH Zürich, CH-8093 Zürich, Switzerland.

[2] Laboratory for Thin Films and Photovoltaics, Empa – Swiss Federal Laboratories for Materials Science and Technology, CH-8600 Dübendorf, Switzerland.

[3] Institute of Advanced Materials (INAM), Universitat Jaume I, 12006 Castelló, Spain.

[4] Materials Theory for Energy Scavenging (MATES) Lab, Harish-Chandra Research Institute (HRI) Allahabad, HBNI, Allahabad, Uttar Pradesh 211019, India.

[5] Yonsei Frontier Lab, Yonsei University, Seoul 03722, South Korea.

[#] These authors contributed equally to this work

*E-mail: rohjohn@ethz.ch, mvkovalenko@ethz.ch

**Supplementary Note 1:**

**Ion diffusion coefficient and T80 data**

In this note we explain in detail the data used to generate Fig. 2c since the reported $D_{ion}$ and $T_{80}$ values are highly dispersed. For this reason, the reported $D_{ion}$ values in Fig. 2c of the main text need to be taken as a qualitative indicator.

For one given perovskite composition, the reported $D_{ion}$ may differ about 1 order of magnitude (or more) depending on the preparation conditions of the perovskite and the analytical technique used to characterize the material as shown in Table SI1. See for example reported values for $MAPbI_3$. Several techniques like those that provide chemical information such as Nuclear magnetic resonance (NMR) experiments or Time-of-flight (ToF) spectroscopies have been used for this purpose. Alternatively, *in-situ* techniques such as Photoluminescence (PL) quenching methods or electrical measurements have also been used. Each technique has its own advantages and limitations. For example, destructive techniques benefit from chemical information but may lack reliability as they need to compare several identical samples. Since sample-to-sample reproducibility is one of the major limiting factors, comparing identical samples is challenging. Alternatively, *in-situ* and non-destructive measurements do not have the required chemical information, and rely on models to extract relevant information. In addition, the reported $D_{ion}$ also depends on the history of the samples, testing conditions (i.e. dark/light, relative humidity or temperature). In any case, the observed trends with cation ion size are consistent across all the techniques and small cations show large values of $D_{ion}$ and large cations lead to small $D_{ion}$. It is also important to note that due to the infinite number of variations in perovskite formulations, for many of them, $D_{ion}$ has not been measured directly for the stability experiments described next. For this reason, formulations have been arranged in groups and a *$D_{ion}$* value has been assigned in the range of the closest formulation for which the data is available.

**Table S1**: Reported $D_{ion}$ measured in the dark for different perovskite materials

| Perovskite composition | $D_{ion}$ / cm$^2$ s$^{-1}$ | Measurement technique | Reference |
|---|---|---|---|
| MAPbBr$_3$ | $1.8 \times 10^{-8}$ | Impedance Spectroscopy | 1 |
| MAPbI$_3$ | $6.0 \times 10^{-8}$ | Current transients | 2 |
| MAPbI$_3$ | $\sim 2 \times 10^{-9}$ | NMR experiments | 3 |
| MAPbI$_3$ | $\sim 5 \times 10^{-9}$ | PL quenching and current transient | 4 |
| MAPbI$_3$ | $2.4 \times 10^{-8}$ | DC polarization | 5 |
| FAPbI$_3$ | $8.0 \times 10^{-9}$ | DC polarization | |
| CsPbI$_3$ | $6.1 \times 10^{-10}$ | DC polarization | |
| MAPbI$_3$ | $2.2 \times 10^{-8}$ | PL quenching and current transient | 6 |
| (FA$_{0.83}$MA$_{0.17}$)$_{0.95}$Cs$_{0.05}$Pb(I$_{0.9}$Br$_{0.1}$)$_3$ | $8.47 \times 10^{-9}$ | PL quenching and current transient | |
| (NMA$_{0.66}$FA$_{0.33}$)PbI$_3$ | $2.2 \times 10^{-10}$ | PL quenching and current transient | |
| (FAPbI$_3$)$_{0.875}$(CsPbBr$_3$)$_{0.125}$ | $8.4 \times 10^{-9}$ | PL quenching and current transient | 7 |
| (PEA)$_2$(MA)$_2$Pb$_3$Br$_{10}$    (n=3) | $8.0 \times 10^{-11}$ | PL quenching | |
| (PEA)$_2$(MA)$_2$Pb$_3$I$_{10}$    (n=3) | $8.0 \times 10^{-12}$ | PL quenching | 8 |
| (PEA)$_2$(MA)$_1$Pb$_2$Br$_7$    (n=2) | $1.0 \times 10^{-12}$ | PL quenching | |
| (PEA)$_2$(MA)$_1$Pb$_2$I$_7$      (n=2) | $2.0 \times 10^{-15}$ | PL quenching | |
| (PEA)$_2$PbBr$_4$          (2D, n=1) | $2.0 \times 10^{-15}$ | PL quenching | |
| (PEA)$_2$PbI$_4$          (2D, n=1) | $5.0 \times 10^{-16}$ | PL quenching | |

Reports for $T_{80}$ are also quite dispersed in the literature. The main reason in this case is that standardized degradation protocols have not been followed in the literature. Only recently, the research community have started to agree on how to report stabilities for perovskite solar cells[9]. For this reason, the $T_{80}$ values selected in this manuscript and summarized in Table SI2 aim to provide experimental conditions that are comparable: degradation at 1 sun illumination at maximum power point with a controlled atmosphere of nitrogen or use of efficient encapsulant (parylene). Unless otherwise stated, all cells show initial PCE >18 %. The control sample configuration is based either on FTO/TiO$_2$/perovskite/Spiro-OMeTAD/Au (n-i-p) or FTO/PEDOT:PSS/Perovskite/PCBM/Ag (p-i-n). Here, modification of the extraction layers, contacts or encapsulation is considered a contacts improvement as opposed to improvements related to the bulk properties of the perovskite.

**Table S2**: Reported $T_{80}$ for different materials.

| Perovskite composition | Improvement | $D_{ion}$ / cm$^2$ s$^{-1}$ (estimated) | $T_{80}$ / h | Reference |
|---|---|---|---|---|
| MAPbI$_3$ | Control sample | $2\times10^{-8}$ | 30 | 10 |
| MAPbI$_3$ | Control sample | $2\times10^{-8}$ | 12 | 11 |
| Cs$_{0.05}$FA$_{0.54}$MA$_{0.41}$Pb(I$_{0.98}$Br$_{0.02}$)$_3$ | Control sample | $2\times10-9$ | 10 | 12 |
| Cs$_{0.05}$FA$_{0.54}$MA$_{0.41}$Pb(I$_{0.98}$Br$_{0.02}$)$_3$ | Control sample | $2\times10^{-9}$ | 30 | 13 |
| Cs$_{0.05}$FA$_{0.54}$MA$_{0.41}$Pb(I$_{0.98}$Br$_{0.02}$)$_3$ | Addition of EDTAK to the ETL | $2\times10^{-9}$ | 125 | |
| Cs$_{0.05}$FA$_{0.54}$MA$_{0.41}$Pb(I$_{0.98}$Br$_{0.02}$)$_3$ | Addition of EDTAK to the ETL and addition of EAMA to Perovskite | $2\times10^{-9}$ | 300 | |
| Cs$_{0.05}$FA$_{0.54}$MA$_{0.41}$Pb(I$_{0.98}$Br$_{0.02}$)$_3$ | ETL+EDTAK and Perovskite + EAMA and mixed Spiro and P3HT | $2\times10^{-9}$ | 2450 | |
| Cs$_5$(FA$_{83}$MA$_{17}$)$_{95}$Pb(I$_{83}$Br$_{17}$)$_3$ | Control sample | $5\times10^{-11}$ | 90 | 14 |
| Rb$_{0.05}$(Cs$_{0.05}$MAFA)Pb(I$_{0.83}$Br$_{0.17}$)$_3$ | Control sample | $5\times10^{-10}$ | 2000 | 14 |

| | | | | |
|---|---|---|---|---|
| $Rb_{0.05}Cs_{0.1}FA_{0.85}PbI_3$ | Use of PMMA in contacts | $5\times10^{-10}$ | 10000 | 15 |
| $(FA_{0.83}MA_{0.17})_{0.95}Cs_{0.05}Pb(I_{0.9}Br_{0.1})_3$ | Control sample with Spiro | $1\times10^{-10}$ | 5 | 10 |
| $Cs_{0.05}FA_{0.54}MA_{0.41}Pb(I_{0.98}Br_{0.02})_3$ | Control sample with Spiro | $1\times10^{-10}$ | 300 | 10 |
| $(MA_{0.15}Cs_{0.09}FA_{0.76})_{0.97}PbI_{2.97}$ | Improved HTL (EH44) | $5\times10^{-11}$ | 1600 | 16 |
| $MA_{0.1}Cs_{0.05}FA_{0.85}Pb(I_{0.95}Br_{0.05})_3$ | Contacts improvement (Use of CuSCN) | $5\times10^{-11}$ | 5000 | 17 |
| $MA_{0.1}Cs_{0.05}FA_{0.85}Pb(I_{0.95}Br_{0.05})_3$ | Control sample | $5\times10^{-11}$ | 50 | 18 |
| $MA_{0.1}Cs_{0.05}FA_{0.85}Pb(I_{0.95}Br_{0.05})_3$ | Extensive contacts improvement | $5\times10^{-11}$ | 10000 | |
| $(MA_{0.15}Cs_{0.09}FA_{0.76})_{0.97}PbI_{2.97}$ | Contact improvement (MoOx) | $5\times10^{-11}$ | 340 | 19 |
| $MA_{0.1}Cs_{0.05}FA_{0.85}Pb(I_{0.95}Br_{0.05})_3$ | Contact improvement (VOx) | $1\times10^{-11}$ | 750 | |
| $MA_{0.1}Cs_{0.05}FA_{0.85}Pb(I_{0.95}Br_{0.05})_3$ | Use of BMIMBF$_4$ and contacts improvement | $1\times10^{-11}$ | 4100 | 20 |
| $MA_{0.1}Cs_{0.05}FA_{0.85}Pb(I_{0.95}Br_{0.05})_3$ | Piperidinium salt and contacts improvement | $1\times10^{-11}$ | 4800 | 21 |
| $(FAPbI_3)_{0.875}(CsPbBr_3)_{0.125}$ | Control sample | $4\times10^{-9}$ | 250 | 7 |
| $(FAPbI_3)_{0.875}(CsPbBr_3)_{0.125}$ | KI doped | $4\times10^{-9}$ | >500 | |
| $(BA)_2(MA)_4Pb_5I_{16}$ | Control sample BA$^+$(n=5) | $5\times10^{-12}$ | 50 | 22 |
| $(MTEA)_2(MA)_4Pb_5I_{16}$ | Improvement large cation Low dimensional (n=5) | $5\times10^{-12}$ | 1000 | |
| $(BA)_2(MA)_3Pb_4I_{13}$ | Low dimensional $^{n=4}$ PCE$_{initial}$= 12 % | $1\times10^{-12}$ | >2500 | 11 |
| $(GA)_2MA_4Pb_5I_{16}$ | Reference 2D perovskite | $5\times10^{-15}$ | 750 | 23 |
| $(GA)_2MA_4Pb_5I_{16}$ | GA on top of perovskite | $5\times10^{-15}$ | 3000 | |

**Supplementary Note 2:**
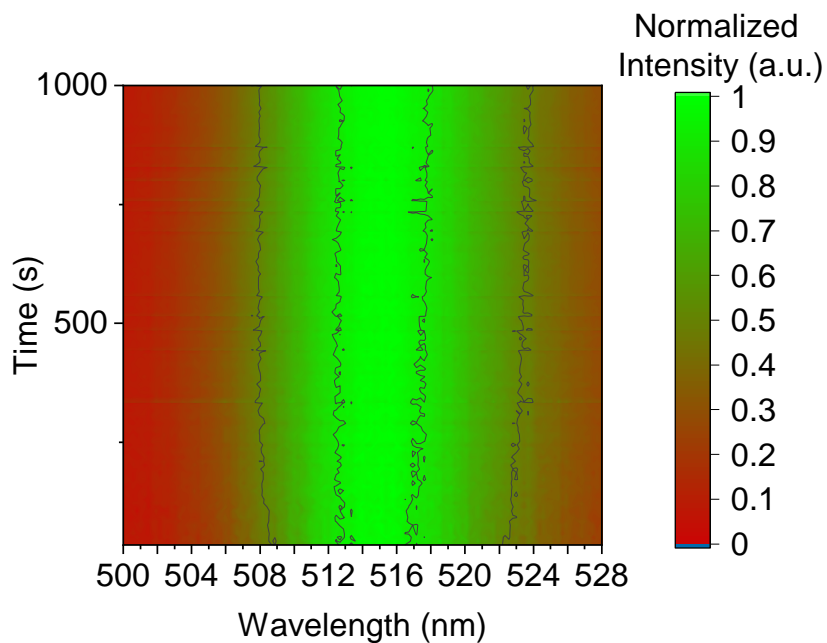


**Figure S1**. Evolution of electroluminescence spectra during pulsed operation of a ITO/PEDOT:PSS/polyTPD/CsPbBr$_3$/B3PYMPM/TPBi/LiF/Al LED. This device is biased at a V$_{base}$ of 3 V to purposefully polarize the device before application of V$_{pulse}$ of 4 V to turn on the LED. The pulse duration used is 200 ms with 20 sec intervals between pulses.
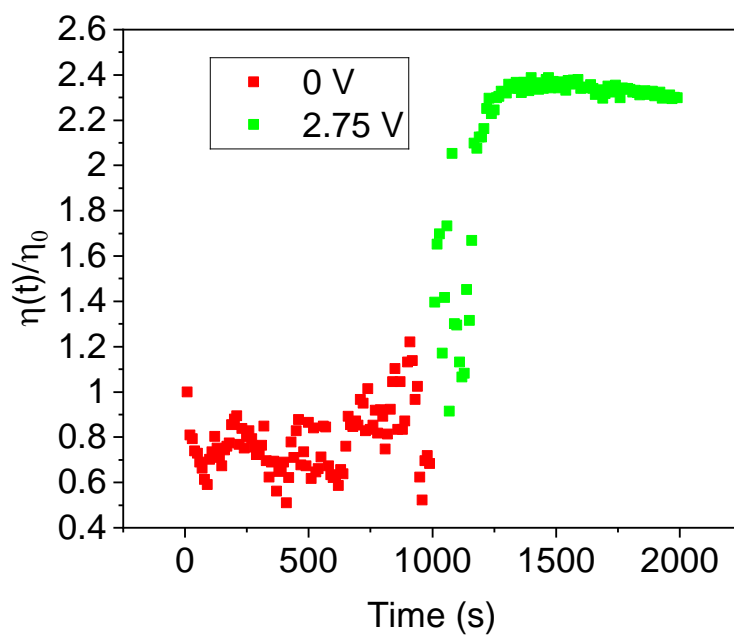


**Figure S2**. Change of normalized electroluminescence upon switching of V$_{bias}$ from 0 to 2.75 V.

The normalization was done by dividing the EL values by the value of the EL measured at the first point (~0 sec)
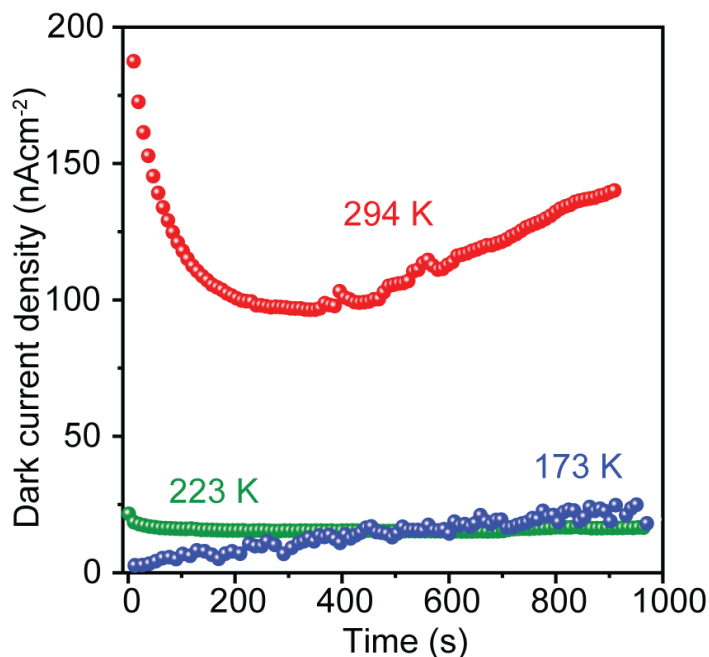
**Supplementary Note 3:**



**Figure S3**. Dark current density-time dependance of a hard radiation detector based on CsPbBr$_3$ SC at different temperatures.

**Supplementary Note 4:**

Due to the many possible configurations and compositions of halide perovskite memristors, it is possible that the different devices show rather different internal mechanisms of operation, and a general picture is far from being obtained. However, we propose a generic description according to the available information. The memristor is characterized by a large rise of the current when a certain voltage threshold is surpassed, showing the transition to a low resistance state (LRS). But the response is dynamic, depending on the kinetic effects as seen by a change of the effective onset voltage as a function of the scan rate. In the reverse scan, the system shows intense hysteresis, as the return pathway stays on the LRS up to reverse voltages that resets the device to a high resistance

state (HRS). These features correspond to complex dynamics that is the combination of several factors: (1) an underlying dc current that defines the HRS, (2) a transition mechanism that forms the LRS. This may consist of the formation of a conductive filament (CF), or the reaction of ions at the interface that removes a Schottky barrier and multiplies the electronic conductivity. This activation necessitates a minimum voltage, in the type of an electrochemical redox potential, to obtain a successful configuration for high conduction. However, this last mechanism necessitates the supply of ions. Hence (3) is an ion displacement that activates the physical transformation leading to LRS. In summary, the memristor behaviour is not univocally controlled by ion migration. This is a necessary component in most cases but is a requisite for a transformational kinetic effect. Understanding the interplay for these factors will be critical for designing memristors of required performance. For example, if the kinetics of the transformation state is slow then one can stop the process and obtain a persistent state of intermediate conductivity, as is required for analog synapses. If the transformation is abrupt, one will obtain instead a binary system. In addition, modulating the ion supply provides a route to control the kinetics of the transformation.

## References

1.     Peng, W. *et al.* Quantification of ionic diffusion in lead halide perovskite single crystals. *ACS Energy Lett.* **3**, 1477–1481 (2018).

2.     García-Batlle, M. *et al.* Mobile ion-driven modulation of electronic conductivity explains long-timescale electrical response in lead iodide perovskite thick pellets. *ACS Appl. Mater. Interfaces* **13**, 35617–35624 (2021).

3.     Senocrate, A. *et al.* The nature of ion conduction in methylammonium lead iodide: a multimethod approach. *Angew. Chemie Int. Ed.* **56**, 7755–7759 (2017).

4.     McGovern, L., Futscher, M. H., Muscarella, L. A. & Ehrler, B. Understanding the stability of MAPbBr3 versus MAPbI3: suppression of methylammonium migration and reduction of halide migration. *J. Phys. Chem. Lett.* **11**, 7127–7132 (2020).

5.     Moia, D. & Maier, J. Ion transport, defect chemistry, and the device physics of hybrid perovskite solar cells. *ACS Energy Lett.* **6**, 1566–1576 (2021).

6.     Li, C., Guerrero, A., Huettner, S. & Bisquert, J. Unravelling the role of vacancies in lead halide perovskite through electrical switching of photoluminescence. *Nat. Commun.* **9**, 1–8 (2018).

7.     Kim, S.-G. *et al.* Potassium ions as a kinetic controller in ionic double layers for hysteresis-free perovskite solar cells. *J. Mater. Chem. A* **7**, 18807–18815 (2019).

8.     Zhang, S. *et al.* Quantifying Anionic Diffusion in 2D Halide Perovskite Lateral

Heterostructures. *Adv. Mater.* **33**, 2105183 (2021).

9.  Khenkin, M. V *et al.* Consensus statement for stability assessment and reporting for perovskite photovoltaics based on ISOS procedures. *Nat. Energy* **5**, 35–49 (2020).

10. Schloemer, T. H. *et al.* Thermally stable perovskite solar cells by systematic molecular design of the hole-transport layer. *ACS Energy Lett.* **4**, 473–482 (2019).

11. Tsai, H. *et al.* High-efficiency two-dimensional Ruddlesden–Popper perovskite solar cells. *Nature* **536**, 312–316 (2016).

12. Domanski, K. *et al.* Migration of cations induces reversible performance losses over day/night cycling in perovskite solar cells. *Energy Environ. Sci.* **10**, 604–613 (2017).

13. Liu, Z. *et al.* A holistic approach to interface stabilization for efficient perovskite solar modules with over 2,000-hour operational stability. *Nat. Energy* **5**, 596–604 (2020).

14. Domanski, K., Alharbi, E. A., Hagfeldt, A., Grätzel, M. & Tress, W. Systematic investigation of the impact of operation conditions on the degradation behaviour of perovskite solar cells. *Nat. Energy* **3**, 61–67 (2018).

15. Turren-Cruz, S.-H., Hagfeldt, A. & Saliba, M. Methylammonium-free, high-performance, and stable perovskite solar cells on a planar architecture. *Science (80-. ).* **362**, 449–453 (2018).

16. Christians, J. A. *et al.* Tailored interfaces of unencapsulated perovskite solar cells for> 1,000 hour operational stability. *Nat. Energy* **3**, 68–74 (2018).

17. Arora, N. *et al.* Perovskite solar cells with CuSCN hole extraction layers yield stabilized efficiencies greater than 20%. *Science (80-. ).* **358**, 768–771 (2017).

18. Zhao, Y. *et al.* A bilayer conducting polymer structure for planar perovskite solar cells with over 1,400 hours operational stability at elevated temperatures. *Nat. Energy* 1–9 (2021).

19. Schloemer, T. H. *et al.* The molybdenum oxide interface limits the high-temperature operational stability of unencapsulated perovskite solar cells. *ACS Energy Lett.* **5**, 2349–2360 (2020).

20. Bai, S. *et al.* Planar perovskite solar cells with long-term stability using ionic liquid additives. *Nature* **571**, 245–250 (2019).

21. Lin, Y.-H. *et al.* A piperidinium salt stabilizes efficient metal-halide perovskite solar cells. *Science (80-. ).* **369**, 96–102 (2020).

22. Ren, H. *et al.* Efficient and stable Ruddlesden–Popper perovskite solar cell with tailored interlayer molecular interaction. *Nat. Photonics* **14**, 154–163 (2020).

23. Huang, Y. *et al.* Stable layered 2D perovskite solar cells with an efficiency of over 19% via multifunctional interfacial engineering. *J. Am. Chem. Soc.* **143**, 3911–3917 (2021).